Full Stall Simulations of a Redesigned Ventilation Fan for the ISS

Branden A. Butler*
University of California Irvine, Irvine, California, 92697

Carlos A. Valentin-Cruz†
Universidad Ana G. Méndez, Recinto de Gurabo, Gurabo, Puerto Rico 00778

Michael R. Borghi Jr.‡ and Mark G. Turner§
NASA Glenn Research Center, Cleveland, Ohio, 44135

The concept of a stall is studied rigorously in the aerospace industry. From a design standpoint, instabilities such as stall are undesirable– operation in the stall regime has a tremendous impact on aerodynamic performance as well as structural integrity. In extreme cases, operating in stall conditions can cause failure. Further, stall can cause a loss of lift on aircraft wings or a loss of thrust in aircraft engines. In any case, stall continues to be a topic of interest in the aerospace industry. The present work aims to show that a ventilation fan, recently designed for the ISS, exhibits behavior at peak pressure and stall that is physically explainable by the Computational Fluid Dynamic (CFD) results. Although the ventilation fan has a rotor-stator design, this paper considers a rotor-only configuration. The FUN3D CFD solver developed by NASA Langley Research Center was used to simulate the operational characteristics of the ventilation fan. FUN3D solves the Unsteady Reynolds-Averaged Naiver-Stokes (URANS) equations using implicit time marching and a dynamic overset grid. The FUN3D solver was originally written for exterior flow fields; however, this work represents an extension of the FUN3D solver to turbomachinery or interior flow fields. The FUN3D results for the rotor-only ventilation fan accurately captured the operational characteristics inherent to compressors– the results shared similar performance trends when compared to the experimental results for the rotor-stator case. A peak adiabatic efficiency of 94% occurred at a MFR of 105.2 CFM, the peak pressure point. A computationally stable stall occurred at a mass flow rate of 43.8 CFM where the adiabatic efficiency dropped to 69%.

Nomenclature

CFD	=	Computational Fluid Dynamics
CFM	=	Cubic Feet per Minute
ISS	=	International Space Station
LE	=	leading edge
MFR	=	Mass Flow Rate
p	=	static pressure
TE	=	trailing edge
RPM	=	Revolution per Minute
SPR	=	Static Pressure Ratio
$URANS$	=	Unsteady Reynolds-Averaged Navier Stokes
u	=	axial velocity
V_r	=	radial velocity
V_θ	=	tangential velocity
W_θ	=	relative tangential velocity

*Ph.D. Student, Aerospace and Mechanical Engineering Department
†Student, Aerospace and Mechanical Engineering Department
‡Research Aerospace Engineer, Turbomachinery and Turboelectric Systems Branch, AIAA Member
§Senior Technologist, Propulsion Division

α = absolute velocity angle
β = relative velocity angle
θ = polar angle
$\overrightarrow{U}$ = rotor wheel speed
$\overrightarrow{V}$ = absolute velocity
$\overrightarrow{W}$ = relative velocity
Δt = non-dimensional time step

I. Introduction

The design of turbomachinery requires extensive numerical and experimental testing to ensure flow instabilities are avoided during all operating conditions. Flow instabilities such as stall can cause a significant decrease in aerodynamic performance, life duration, and propulsive efficiency due to flow reversal, flow blockage and structural vibration [1]. As a result, numerous studies have looked into stall as a means to predict the resulting flow behavior and the stability limit of various turbomachinery configurations. Prior studies relied on simplified model-based experiments due to hardware and numerical limitations. More recently, numerical models are becoming more attractive due to computing power and software advances. Although advancements have been made from a numerical standpoint, the concept of simulating stall has its own difficulties. The unsteady flow field requires a time-accurate, nonlinear, and viscous flow representation. Additionally, the flow field requires a turbulence model capable of resolving flow separation and reattachment [2], [3].

Numerous experiments have identified the precursors of stall. In [4], a pseudo-correlation integral method (i.e., the correlation method) was used to identify stall precursive events in the pressure fluctuations measured from pressure transducers located at the front of various compressor rigs. It was concluded that the correlation method successfully identified the onset of stall for four different compressor configurations. Similarly, [5] applied a correlation-based scheme to identify a measure that captures momentary lapses in flow behavior prior to the onset of aerodynamic instabilities. The data relied on pressure sensors mounted over the rotor for three compressor configurations.

More recently, investigations on the phenomena of stall have shifted towards numerical simulation. Unlike experiments, computations enable control over the complete domain of interests and are more affordable. Previous computational studies have simulated stall by either specifying a constant radial back pressure or using a variable nozzle approach. In [2], it was found that the variable nozzle approach is well-suited for compressor simulations past the stall point. Beyond the stall point, the flow becomes genuinely unsteady and the imposition of a radially constant exit pressure may lead to numerical instabilities. A similar approach was applied in [6] which predicted the aerodynamic performance of a NASA Stage35 single-stage compressor configuration. To simulate an entire speed line, from choke through stall, the nozzle area was modified to achieve a specific mass flow rate (MFR).

The flow code, FUN3D, is an unsteady flow solver which solves the Unsteady Reynolds-Averaged Navier Stokes (URANS) equations. The code applies implicit time marching and dual time stepping to ensure time accuracy. Additionally, the Spalart-Allmaras (SA) turbulence model was the turbulence model of choice for the following computations. Rather than applying the variable area nozzle approach, a full speed-line was captured by varying the fan back pressure. Since the flow phenomena beyond stall was not considered, the numerical instabilities suggested in [2] were avoided. The intent of this paper is to achieve the following two objectives: (1) to show that the ventilation fan exhibits behavior at peak pressure and stall that is physically explainable by the FUN3D results, and (2) to demonstrate that FUN3D is capable of resolving the operational characteristics inherent to compressors. The following sections will compare the rotor-only simulation results with the rotor-stator experimental results to ensure that the computational model accurately resolves the operational characteristics of the ventilation fan.

II. Fan Configuration

This paper will predict the aerodynamic performance of a cabin ventilation fan designed for the International Space Station (ISS). The ventilation fan was specifically designed to improve aerodynamic and acoustic performance. Figure 1 shows the meridional and three-dimensional views of the full stage (i.e., rotor-stator) ventilation fan. The configuration is composed of nine rotor blades and eleven stator blades. The ventilation fan has a 100% design speed of 12,000 RPM, an outer diameter of 0.08 meters, and an approximate tip clearance of 0.0002 meters [7]. The fan is designed and tested to pull stationary air in from the surrounding environment. At the peak operating efficiency the mach number at the inlet

is approximately 0.033. The computational results presented herein consider a rotor-only configuration and matched the experimental inlet conditions.

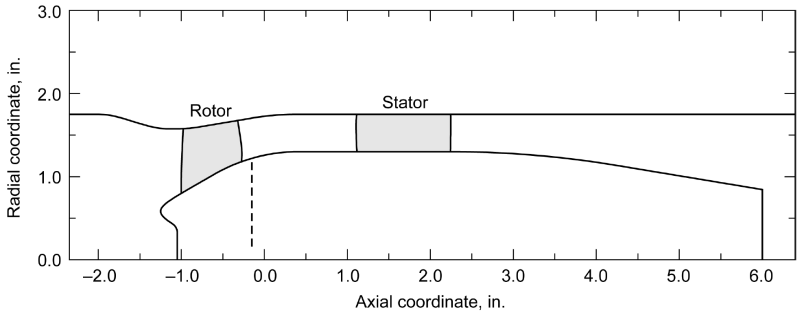

(a) Meridional view

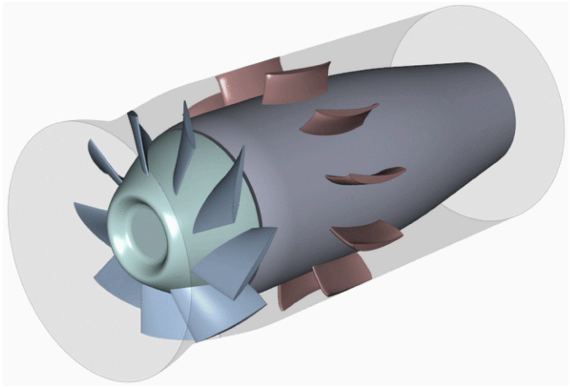

(b) Three-dimensional view

Fig. 1 Ventilation fan test case [7].

III. Numerical Simulation

The FUN3D flow solver was used for the simulations presented herein. FUN3D solves the URANS equations by applying an unstructured node-based finite volume discretization on a dual-mesh. The solution algorithm is based on a point implicit time integration technique coupled with local time-stepping and temporal error controllers. The popular and robust one-equation Spalart-Allmaras (SA) turbulence model[8] was used to solve for the kinematic eddy turbulent viscosity. Parallel decomposition with Message Passage Interface (MPI) communication is also supported for distributed computing.

While FUN3D has extensive history of use in rotorcraft simulations[9, 10] it is has not historically been applied to turbomachinery problems. There is a desire to take advantage of the many advanced solver features (i.e., adjoint design optimization and fluid-solid interaction) which already exist within the code for future work. This work is part of the first steps of evaluating the FUN3D flow solver for turbomachinery applications.

For rotorcraft simulations in FUN3D, an overset grid approach is typically applied. For this first step towards tubomachinery in FUN3D, overset grids were not used in favor of a single rotating mesh. This allowed the focus of the work to be on the solver numerics and leaves the rigorous detail required to obtain a high quality overset interpolation - particularly within the tip clearance of the rotor - to a future ongoing work. The full annulus of the ventilation fan rotor was taken meshed as a single domain extending from the start of the inlet (-2 in. in Fig 1a) to the location of the stator leading edge. The stator was not included in this simulation. The URANS equations were solved in the inertial frame, requiring a dynamic (i.e., moving) grid to simulate the rotor rotation. The inflow boundary conditions held total pressure and temperature constant at levels matching the ambient reference conditions (i.e., $P_o = T_o = 1.0$) shown in Table 1. The outflow boundary was applied as a uniform static pressure, and was varied to adjust the mass flow rate. Viscous, adiabatic walls were applied to the rotor hub and rotor blades. While, free slip adiabatic walls were applied to

Table 1 Input Refence conditions and corresponding physical values used for FUN3D simulations

Input Reference Values	
M_{ref}	0.033
Re_{ref}	754,000
$T_{ref}[K]$	294.3
Corresponding Physical Conditions	
P [kPa]	102.07
$\rho[kg/m^3]$	1.21

the casing to not induce swirl from the rotating casing. Currently, the only implemented approach to account for the relative motion between a rotor and the case is with overset grids. A separate work is underway to add sliding interfaces and multiple relative reference frames to FUN3D is currently underway. All of the operating points simulated herein were fixed at the design speed of 12,000 RPM.

In order to ensure sufficient grid resolution was provided along the hub, hub nose, and the blade boundaries, y+ values were plotted for the two operating conditions considered in this paper: (1) the peak pressure point (105.2 CFM), and (2) the computationally stable stall point (43.8 CFM). As seen in Eq. 1, y+ is proportional to the shear velocity (u_τ) in Eq. 2.

$$y+ = \frac{y u_\tau}{\nu} \tag{1}$$

$$u_\tau = \sqrt{\frac{\tau_w}{\rho}} \tag{2}$$

The y+ contours can be seen in Fig. 3 for both operating conditions. It is clear that a fine grid is required along the hub aft of the rotor passage, and along the Leading Edge (LE) and Trailing Edge (TE) of the rotor blade at each operating condition. Figure 2 shows the resulting unstructured grid that was generated via Pointwise for the rotor-only ventilation fan. The mesh has a total cell count of 3.2 million nodes. Fig. 2a shows the outer casing mesh, whereas Fig. 2b and Fig. 2c show the full annulus rotor mesh and a zoomed-in view of the rotor mesh, respectively. The non-dimensional time-step was ($\Delta\tau$) of 0.01, which corresponds to 172 time-steps per revolution. Since no relative motion was being resolved, a larger time-step was possible for this pseudo-steady state. The mean flow CFL was ramped from 1.10 and 50 across 20 sub-iterations followed by 10 more sub-iterations at a CFL of 50. The turbulent CFL was ramped from 1.1 to 30 over 20 sub-iterations followed by 10 more sub-iterations at a CFL of 30.

IV. Results

A. Computational and Experimental Speed-lines

Different back pressures were considered in FUN3D to adjust the Mass Flow Rate (MFR) and obtain a speed-line at the 100% design speed, 12,000 RPM. The Static Pressure Ratio (SPR) ranged between 1.0037 to 1.0076. These SPRs resulted in MFR values between 161.1 CFM and 43.8 CFM, respectively. Figure 4 shows a comparison between the computational and experimental results for total pressure rise as a function of MFR at the 100% design speed. The experimental results considered a rotor-stator configuration and the relative motion between the rotor and casing, leading to lower total pressure values when compared to the computational results. Further, the inclusion of a stator and the relative motion between the rotor and hub induces additional flow losses (e.g., swirl) and therefore total pressure loss when compared to the rotor-only case. Despite these differences, the computational results accurately captured the operational characteristics inherent to compressors. The peak pressure MFR for the computational results was 105.2 CFM, whereas the peak pressure MFR for the experimental results was 110.3 CFM. The computational stall MFR was found to be 43.8 CFM as opposed to 97.7 CFM in the experiment. Based on these trends, it is clear that the computational MFR values are less than the experimental MFR values at all total pressure ratios. In other words, the computational speed-line is shifted to the left, indicating that the blade loading, or the amount of work extracted from the blade, is more significant for the rotor-only case. This is expected since the computations are based on set SPRs.

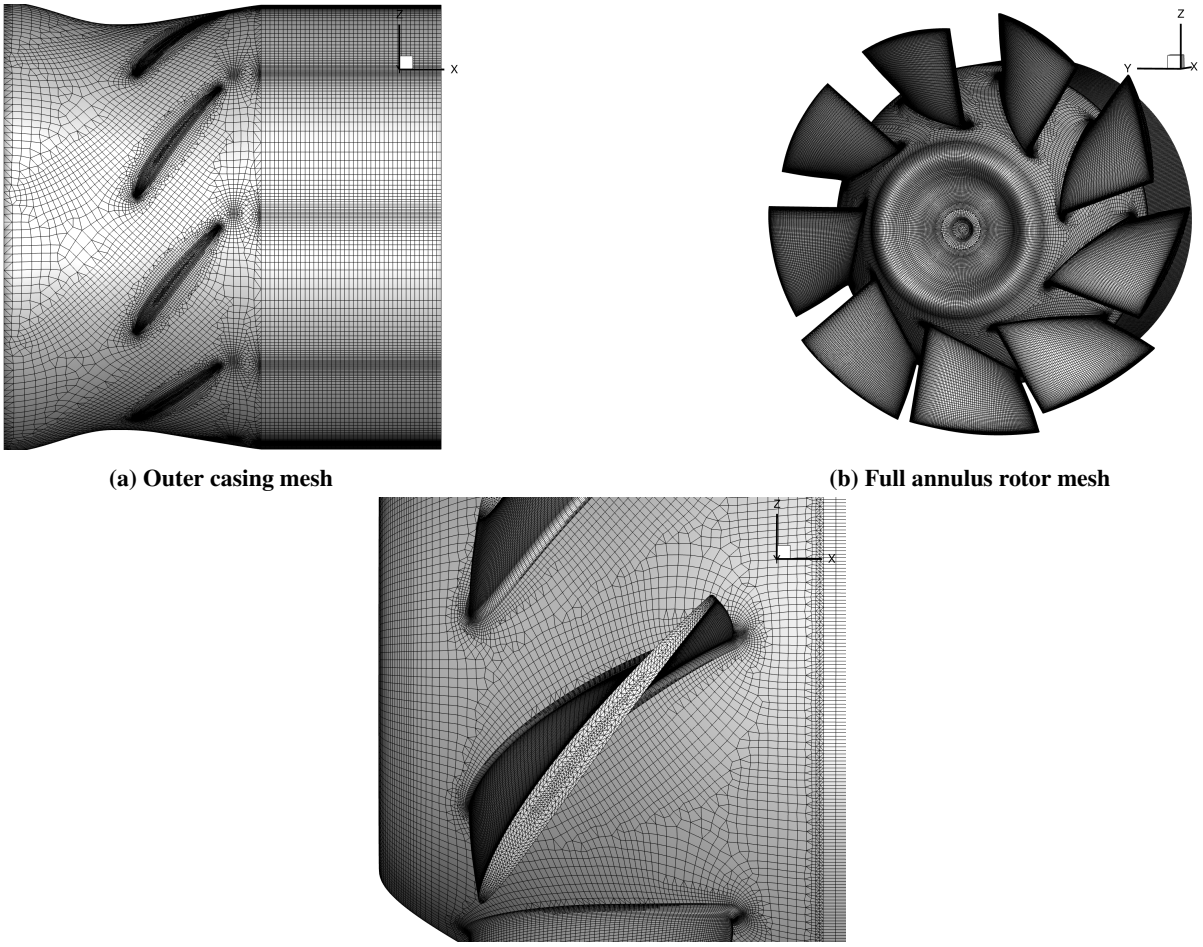

(a) Outer casing mesh

(b) Full annulus rotor mesh

(c) Zoomed-in view of the rotor mesh

Fig. 2 Unstructured mesh used for the rotor-only ventilation fan.

To achieve a specific SPR, the blade loading for the rotor-only configuration is expected to be greater than that of the rotor-stator configuration, shifting the computational MFR values to the left. This accounts for the 55% difference between the computational and experimental stall MFRs. Figure 5 shows the computational results for the adiabatic efficiency. The adiabatic efficiency was 94% at the peak pressure point and dropped to 69% at the computationally stable stall point. We see that the stall point, which results from an SPR of 1.0076, experiences a significant loss in adiabatic efficiency. Performance degradation of this magnitude suggests significant unsteady behavior at the stall point– the flow phenomena resulting in this performance drop will be discussed in the following sections.

B. Stall Static Pressure Ratio

To search for the computationally stable stall point, the static pressure ratio (SPR) was varied from 1.0037 to 1.0076. The resulting mass flow rate (MFR) varied between 161.1 CFM and 43.8 CFM, respectively. Several convergence plots were generated at each SPR to identify the computationally stable stall point. At an SPR of 1.007585 the MFR stabilized at 105.2 CFM. Figure 6 shows the transient response of MFR as a function of simulation time when the SPR was increased slightly from 1.007585 to 1.0076. The resulting MFR was initially stable when the simulation time was less than 120; however, the MFR dropped by nearly 60% as the simulation time increased to 128. Beyond this point, the MFR stabilized at 43.8 CFM. The 60% drop in MFR indicates flow blockage which is a characteristic of stall. Therefore, it was concluded that an SPR of 1.0076 resulted in the computationally stable stall MFR, 43.8 CFM. An SPR of 1.007585 resulted in the peak pressure MFR, or the minimum aerodynamically stable MFR, 105.2 CFM. From this point on, 105.2 CFM will be referred to as the peak pressure point, whereas 43.8 CFM will be referred to as the

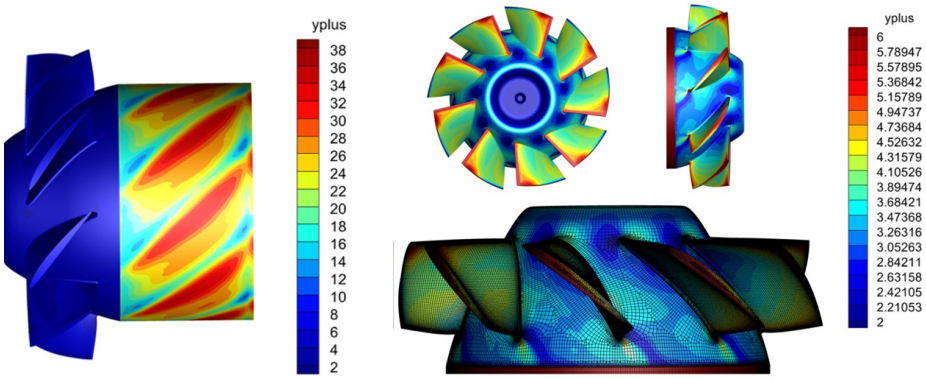

(a) 105.2 CFM

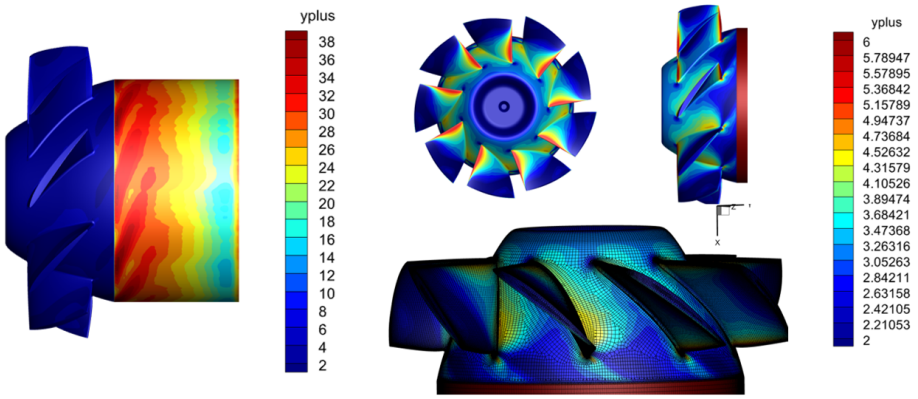

(b) 43.8 CFM

Fig. 3 Y-Plus contours at the peak pressure and computationally stable stall points.

computationally stable stall point.

C. Demonstration of Velocity Components

The FUN3D solver solves the Navier Stokes equations in the inertial frame and computes the absolute velocity:

$$\overrightarrow{V} = u\hat{i} + v\hat{j} + w\hat{k} \tag{3}$$

As part of the analysis, the absolute velocities were converted to the tangential (V_θ) and radial (V_r) velocities to study flow separation at the stall point. Additionally, the absolute velocity ($\overrightarrow{V}$) was converted to the relative velocity ($\overrightarrow{W}$) for ease of visualization. Unlike the absolute velocity which has a velocity angle, α, with respect to the axial direction, the relative velocity is in the rotating frame (i.e., rotor frame) and has a velocity angle, β, with respect to the axial direction. Therefore, a change in β can be viewed as a change in the angle of attack of the rotor. The distinction between the absolute and relative velocities can be viewed further in Fig. 7. The equations used for said conversions were partially retrieved from Gutzwiller et al, [11]. The absolute velocity ($\overrightarrow{V}$), relative velocity ($\overrightarrow{W}$), and rotor wheel speed ($\overrightarrow{U}$) were

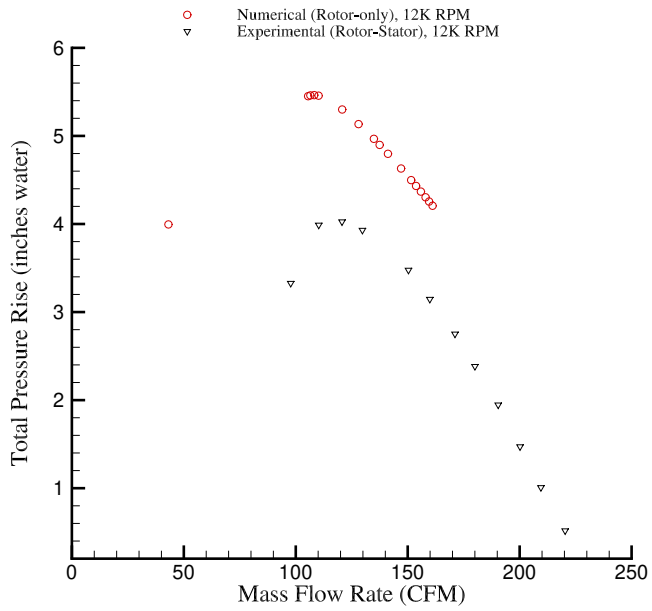

Fig. 4 Comparison between the experimental and computational speed-lines.

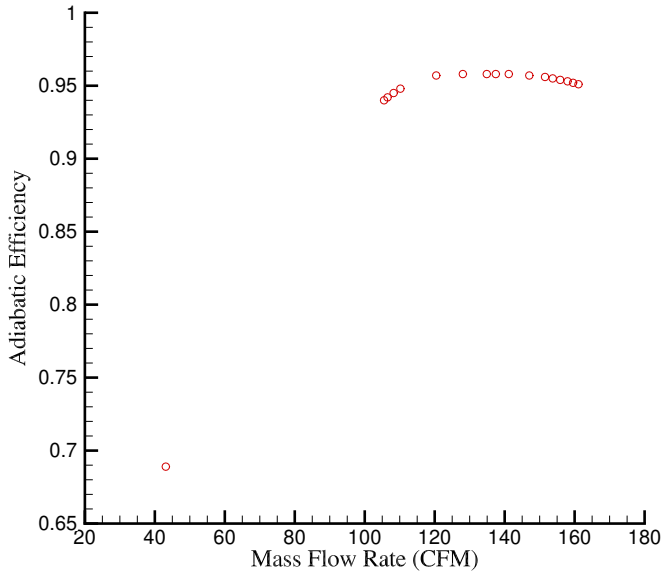

Fig. 5 Computational results for adiabatic efficiency as a function of mass flow rate.

used in the following equations.

$$\vec{V} = \vec{W} + \vec{U} \tag{4}$$

$$\vec{V} = u\hat{i} + V_r\hat{i_r} + V_\theta\hat{i_\theta} \tag{5}$$

$$\vec{W} = W_x\hat{i} + W_r\hat{i_r} + W_\theta\hat{i_\theta} \tag{6}$$

$$W_x = u;\ W_r = V_r \tag{7}$$

$$\vec{U} = \vec{\Omega} \times \vec{r} = \omega r\hat{i_\theta} \tag{8}$$

$$W_\theta = V_\theta - U = V_\theta - \omega r \tag{9}$$

$$V_r = u\cos\theta + w\sin\theta \tag{10}$$

$$V_\theta = -u\sin\theta + w\cos\theta \tag{11}$$

$$\tan\alpha = V_\theta/u \tag{12}$$

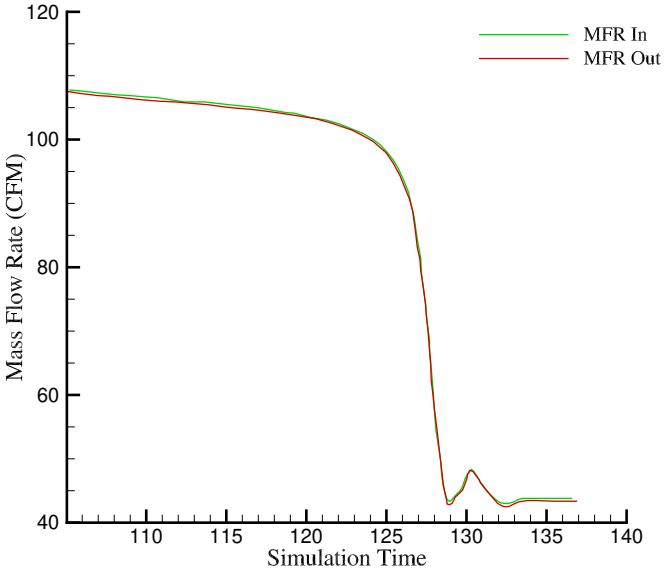

Fig. 6 Transient response of MFR when the SPR is increased from 1.007585 **to** 1.0076**.**

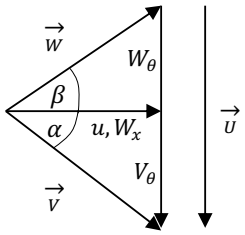

Fig. 7 Velocity triangle relating the absolute ($\vec{V}$), relative ($\vec{W}$), and rotor wheel ($\vec{U}$) velocities.

D. Post-processed Results

The mass flow rates (MFR), 105.2 and 43.8 CFM, are linked to the peak pressure point and the computationally stable stall point, respectively. For both MFR, the computational results were post-processed to visualize the distribution of several variables of interest. These variables of interests include static pressure (p), axial velocity (u), tangential velocity (V_θ), radial velocity (V_r), and the absolute and relative velocity angles (α, β). Each variable is normalized by set reference values in the FUN3D solver. In order to display the rotor blades in two dimensions, a cylinder sample was extracted from the computational domain at the trailing edge (TE) mid-span of the ventilation fan. Figure 8 shows the cylinder with respect to the ventilation fan. This cylinder was unwrapped in the circumferential direction to form two-dimensional contours for the variables of interest. The intent is to show the capabilities of the FUN3D solver, and to justify the computational results for the speed-line presented in Fig. 4.

1. Streamlines

As can be seen in Fig. 5, there is a significant drop in adiabatic efficiency between the peak pressure point (105.2 CFM) and the computationally stable stall point (43.8 CFM). To better understand the differences between the two points, Fig. 9 shows the streamlines for both cases in the relative frame. In Fig. 9a, the streamlines at the peak pressure point are displayed. At this point, the flow upstream of the rotor leading edge (LE) has a relative velocity angle (β) magnitude of approximately 70°. It is clear that the flow remains attached at this velocity angle and the performance

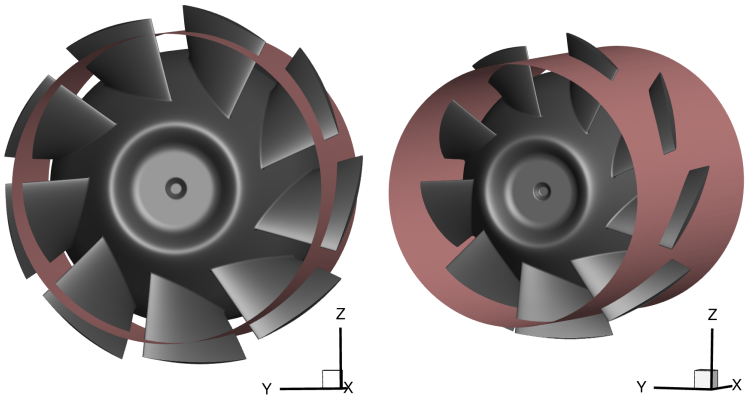

Fig. 8 Trailing Edge (TE) mid-span cylinder sample extracted from the computational domain.

losses inherent to stall are avoided. Fig. 9b shows the streamlines at the computationally stable stall point. The relative velocity angle increases to a magnitude of approximately 95°, causing flow separation and flow reversal along the upper (i.e., suction) surface of the rotor blade. As a result, the stall point experiences significant performance degradation when compared to the peak pressure point.

(a) Minimum Stable MFR (105.2 CFM) **(b) Stall Point (43.8 CFM)**

Fig. 9 Relative velocity (W_θ, W_x) streamlines.

2. Static Pressure Contours

As mentioned previously, a cylinder sample was extracted and unwrapped circumferentially to display the contour plots in two dimensions. The two dimensions in the results to follow are the tangential coordinate (θ) and the axial coordinate ($-X/R$) where R is the radius of the extracted cylinder. Figure 10 shows the two-dimensional static pressure contours at the peak pressure point (105.2 CFM) and the computationally stable stall point (43.8 CFM). As expected, we see a static pressure increase across the rotor passage for both cases. In Fig. 10a, the peak pressure point, we see a gradual increase in static pressure along the suction surface of the rotor blade. On the contrary, Fig. 10b shows a relatively constant static pressure along the suction surface at the stall point. Additionally, the static pressure upstream of the rotor LE increases during stall. This can also be seen in Fig 11 which shows the blade loading, or the distribution of static pressure along the rotor blade surface. The top line is the distribution of static pressure along the suction surface of the rotor blade, whereas the bottom line is the distribution of static pressure along the pressure surface of the rotor blade. It is clear that the blade loading, or the work extracted from the blade, is more significant at the peak pressure point– the minimum static pressure at the rotor LE is approximately 0.697 at this point, and increases to approximately 0.715 at the stall point. Aft of the rotor LE, the static pressure along the suction surface increases gradually at the peak

pressure point, whereas the static pressure remains constant during stall. The flow above the rotor becomes independent from the the freestream during stall, resulting in a constant static pressure along the suction surface of the the rotor blade. This can also be seen in the streamline plots in Fig. 9b. Unlike Fig. 9a, the flow reversal at stall prevents the freestream from passing through the rotor passage. This in turn decreases the blade loading at the computationally stable stall point, reducing the work transmitted from the blade to the flow. As a result, the adiabatic efficiency drops significatly at the stall point as was seen in Fig. 5.

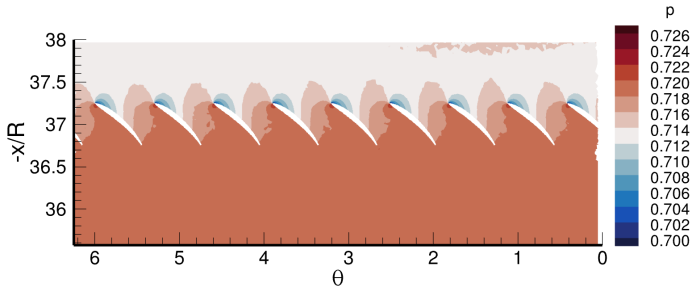

(a) 105.2 CFM

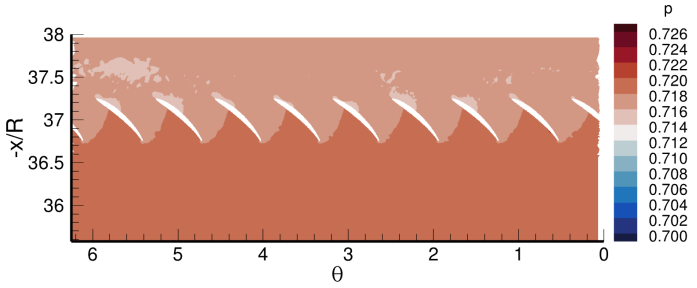

(b) 43.8 CFM

Fig. 10 Static pressure contour at the rotor mid-span.

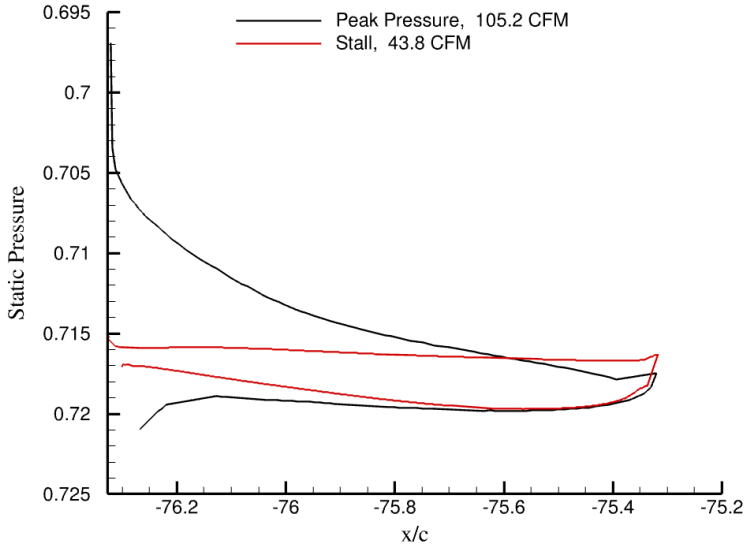

Fig. 11 Blade loading at the peak pressure and stall point.

3. Axial Velocity Contours

To better understand the performance degradation between the peak pressure point and the computationally stable stall point, Fig. 12 shows the axial velocity (u) contours at both operating conditions. The axial velocity can be used to identify regions of flow reversal, or regions where the axial velocity becomes less than zero ($u < 0$). Comparing the two cases using the same scale in Fig. 12, we see that the computationally stable stall point (43.8 CFM) experiences flow reversal along the suction surface of the rotor (refer to Fig. 12b). Additionally, there is flow reversal upstream of the rotor LE which indicates flow blockage, preventing the free stream from passing through the rotor passage. As mentioned in the previous section, this flow behavior increases the static pressure upstream of the rotor LE and results in a constant static pressure along the suction surface of the rotor. On the contrary, the axial velocity at the peak pressure point (105.2 CFM) is positive in all regions aside from the stagnation point (refer to Fig. 12a). The adverse effects of stall, such as flow reversal and flow blockage, are absent at this operating condition.

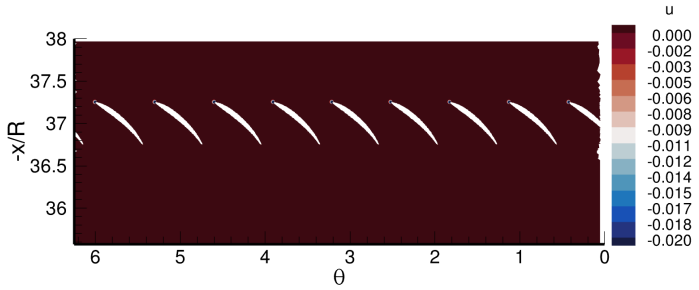

(a) 105.2 CFM

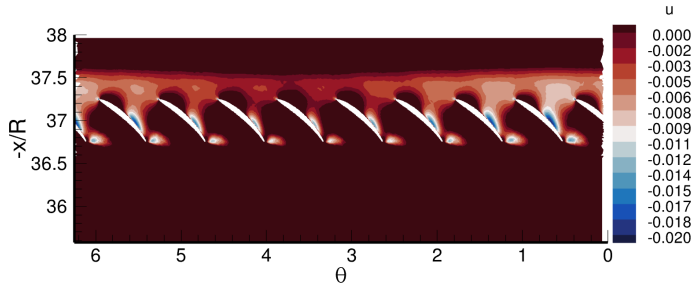

(b) 43.8 CFM

Fig. 12 Axial velocity contour at the rotor mid-span.

4. Radial and Tangential Velocity Contours

The radial (V_r) and tangential (V_θ) velocity components were calculated for both the peak pressure point (105.2 CFM) and the computationally stable stall point (43.8 CFM). From Eq. 7 we see that the radial velocity does not change between the absolute and relative frame ($V_r = W_r$). Therefore, the radial velocity can be viewed as the span-wise flow across the rotor. A positive radial velocity ($V_r > 0$) indicates span-wise flow towards the casing, whereas a negative radial velocity ($V_r < 0$) indicates span-wise flow towards the hub. As the flow field becomes unsteady at stall, the pressure gradients in the span-wise direction increase, leading to larger values of radial velocity. This can be seen in Fig. 13 which shows the radial velocity contours at both operating conditions. The magnitude of radial velocity at the peak pressure point (Fig. 13a) is much less than that at the computationally stable stall point (Fig.13b). Further, the flow blockage resulting from stall forces the flow toward the hub along the suction side of the rotor as indicated by high negative radial velocity values. Along the pressure side of the rotor, the flow is forced towards the casing as indicated by the high positive radial velocity values.

The tangential velocity (V_θ) was also plotted for the peak pressure and computationally stable stall points. Unlike the radial velocity, positive ($V_\theta > 0$) and negative ($V_\theta < 0$) tangential velocities indicate right and left motion in Fig. 14, respectively. Upstream of the rotor LE, the tangential velocity is nearly zero at the peak pressure point as the freestream is not disturbed (Fig. 14a). On the contrary, Fig. 14b shows significant right-moving flow upstream of the rotor LE. Further, the flow blockage at stall forces the flow to the right, preventing the freestream from passing through the rotor

passage. Within the rotor passage, the low tangential velocity at the peak pressure point indicates that that the flow is being turned properly by the rotor blades; however, the high tangential velocity at the stall point indicates that the rotor blades are ineffective in turning the flow, and the stall cells are being carried at the blade speed.

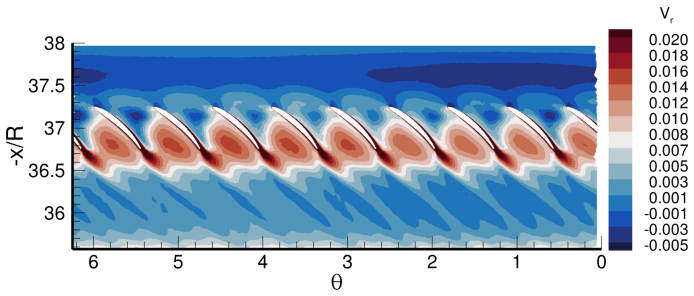

(a) 105.2 CFM

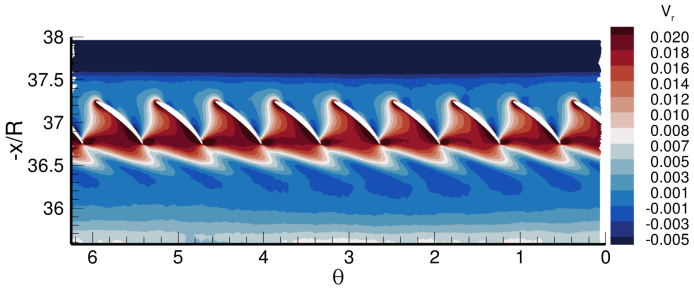

(b) 43.8 CFM

Fig. 13 Radial velocity contour at the rotor mid-span.

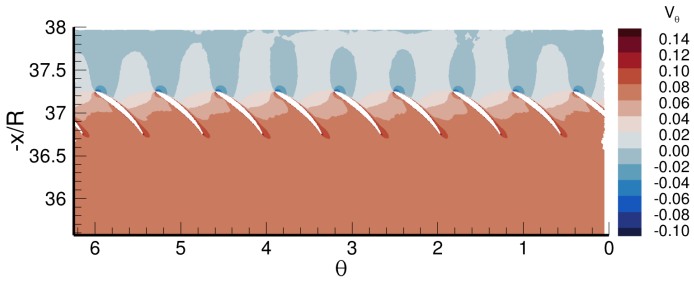

(a) 105.2 CFM

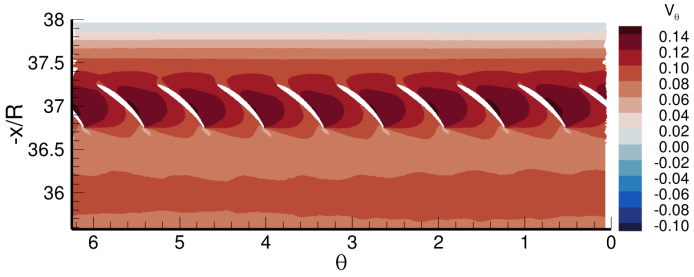

(b) 43.8 CFM

Fig. 14 Tangential velocity contour at the rotor mid-span.

5. Absolute and Relative Velocity Angle Contours

The absolute (α) and relative (β) velocity angles were plotted for the 105.2 and 43.8 CFM cases and are shown in Fig. 15 and Fig. 16, respectively. The absolute velocity angle (α) is the velocity angle in the inertial (i.e., stationary) frame. Figure 15a shows the absolute velocity contour at the peak pressure point, 105.2 CFM. At this point, flow reversal has not occurred and the absolute velocity angle upstream of the rotor LE is approximately 0°. At the stall point, Fig. 15b shows that the absolute velocity angle upstream of the rotor LE jumps to nearly 90°. The flow blockage resulting from the flow separated regions induces flow reversal and reduces the work transmitted from the rotor to the flow field. As a result, the flow upstream of the rotor LE propagates parallel to the plane of rotation, or an absolute velocity angle of 90°.

The relative velocity angle (β) is the velocity angle in the rotating (i.e., rotor) frame. As seen in Fig. 7, a change in the relative velocity angle can be viewed as a change in the angle of attack of the rotor. Much like an airfoil, we expect a critical relative velocity angle that induces flow separation, recirculation, and stall. Figure 16a shows the relative flow angle at the peak pressure point. At this point, the relative flow angle upstream of the rotor LE is approximately $-70°$ and increases in value when passing through the rotor passage. The relative flow angle remains negative since there is no flow reversal when operating at this point. When the MFR drops to 43.8 CFM, the relative flow angle upstream of the rotor LE jumps to approximately $-95°$ at the computationally stable stall point. Much like an airfoil, the relative flow angle jumps significantly leading to flow separation and recirculation. The recirculation zones occur along the suction surface of the rotor when the relative velocity switches from a negative to a positive value.

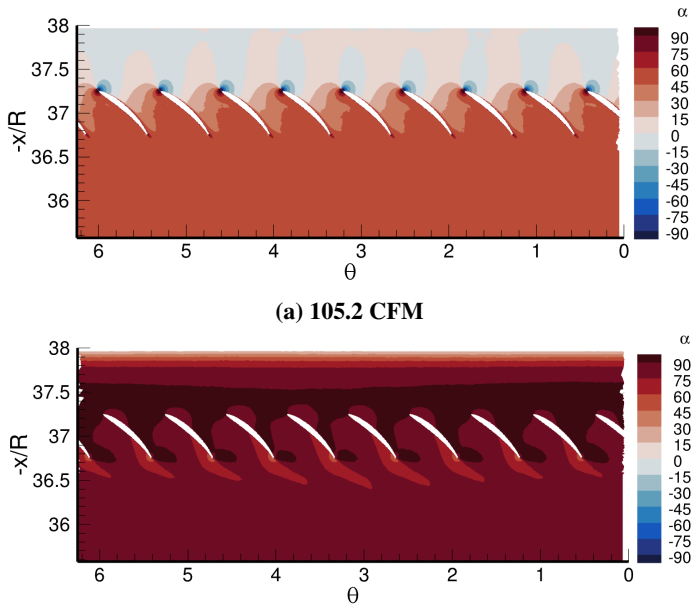

(a) 105.2 CFM

(b) 43.8 CFM

Fig. 15 Absolute velocity angle (α) contour at the rotor mid-span.

V. Conclusion

Simulations of a rotor-only ventilation fan were carried out in FUN3D to achieve the following two goals: (1) to show that the ventilation fan exhibits behavior at peak pressure and stall that is physically explainable by the FUN3D results, and (2) to demonstrate that FUN3D is capable of resolving the operational characteristics inherent to compressors. The rotor-only computations solved the URANS equations using a dynamic grid and the Spalart-Allmaras (SA) turbulence model. A series of static pressure ratios (SPRs) were implemented in FUN3D to capture a full speed-line at the 100% design speed. It was found that an SPR of 1.007585 led to the peak pressure MFR, 105.2 CFM. As the SPR increased to 1.0076, the computationally stable stall point was achieved and the MFR dropped to 43.8 CFM. The adiabatic efficiency was also calculated and dropped from 94% to 69%, respectively. To validate the numerical algorithm, the total pressure rise was compared between the rotor-only computational results and the rotor-stator experimental results. Since the

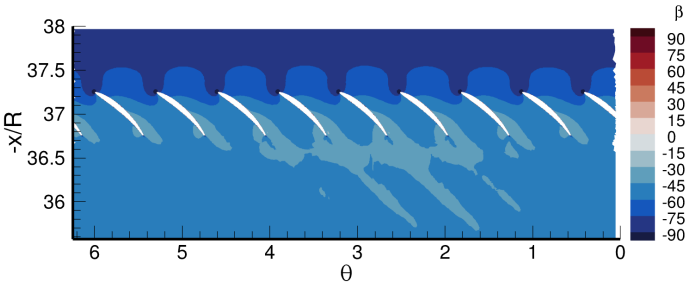

(a) 105.2 CFM

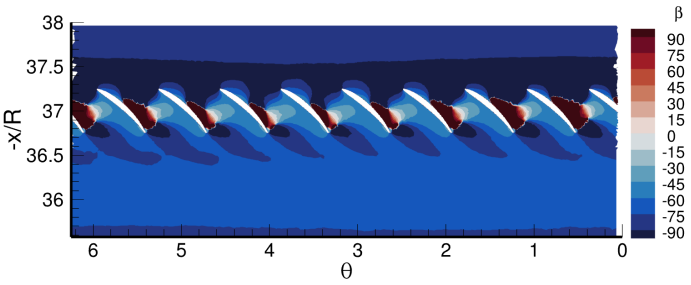

(b) 43.8 CFM

Fig. 16 Relative velocity angle (β) contour at the rotor mid-span.

experimental results considered a stator and the relative motion between the rotor and casing, the flow losses were greater and the rise in total pressure was less than that of the computational results. The experimental peak pressure MFR was 110.3 CFM and the stall MFR was 97.8 CFM. The computational speed-line was shifted to the left as the rotor-only computations were based on a specified back pressure– the blade loading for the rotor-only configuration is expected to be greater than that of the rotor-stator configuration. A series of contour, axial, and streamline plots were post-processed to visualize and verify the computational results and performance trends. Overall, it was concluded that the FUN3D results at the peak pressure and stall point were physically explainable. The details obtained from the preceding simulations offer hope in the investigation of stall and the extension of FUN3D to a turbomachinery flow solver.

Acknowledgments

Special thanks to Alejandro Claro, Timothy Beach, Ali Ameri, Gregory Heinlein, and the FUN3D team at NASA Langley Research Center for assisting me in the learning process of the complex journey of CFD simulations and for the long hours invested to help me understand the relevant software. Another thanks to NASA Glenn Research Center for accepting me as an intern for the past two summers and providing me with the opportunity to expand my knowledge in Computational Fluid Dynamics and Turbomachinery.

References

[1] Gourdain, N., Burguburu, S., Leboeuf, F., and Michon, G. J., "Simulation of rotating stall in a whole stage of an axial compressor," *Computers Fluids*, Vol. 39, No. 9, 2010, pp. 1644–1655. https://doi.org/https://doi.org/10.1016/j.compfluid.2010.05.017, URL https://www.sciencedirect.com/science/article/pii/S0045793010001313.

[2] Vahdati, M., Sayma, A. I., Freeman, C., and Imregun, M., "On the Use of Atmospheric Boundary Conditions for Axial-Flow Compressor Stall Simulations," *Journal of Turbomachinery*, Vol. 127, No. 2, 2004, pp. 349–351. https://doi.org/10.1115/1.1861912, URL https://doi.org/10.1115/1.1861912.

[3] Choi, M., and Vahdati, M., "Numerical strategies for capturing rotating stall in fan," *Proceedings of the Institution of Mechanical Engineers, Part A: Journal of Power and Energy*, Vol. 225, 2011, pp. 655–664. https://doi.org/10.1177/0957650911403869.

[4] Bright, M. M., Qammar, H. K., Weigl, H. J., and Paduano, J. D., "Stall Precursor Identification in High-Speed Compressor Stages Using Chaotic Time Series Analysis Methods," *Journal of Turbomachinery*, Vol. 119, No. 3, 1997, pp. 491–499. https://doi.org/10.1115/1.2841148, URL https://doi.org/10.1115/1.2841148.

[5] Dhingra, N. Y., M., and Prasad, J., "Stall and Surge Precursors in Axial Compressors," *American Institute of Aeronautics and Astronautics*, 2003.

[6] Davis, R., and Yao, J., "Prediction of Compressor Stage Performance from Choke Through Stall," *Journal of Propulsion and Power*, Vol. 22, No. 3, 2006, pp. 550–557. https://doi.org/10.2514/1.15463, URL https://doi.org/10.2514/1.15463.

[7] Tweedt, D. L., "Aerodynamic Design and Computational Analysis of a Spacecraft Cabin Ventilation Fan," *NASA Technical Reports*, 2010.

[8] Spalart, P. R., and Allmaras, S. R., "A One-Equatlon Turbulence Model for Aerodynamic Flows," AIAA Paper 1992-0439, 1992.

[9] Biedron, R. T., and Lee-Rausch, E. M., "Rotor Airloads Prediction Using Unstructured Meshes and Loose CFD/CSD Coupling," AIAA Paper 2008-7341, 2008.

[10] Wang, L., Diskin, B., T., B. R., J., N. E., and Bauchau, O. A., "High-Fidelity Multidisciplinary Sensitivity Analysis and Design Optimization for Rotorcraft Applications," , 2019.

[11] *Educational Software for Blade and Disk Design*, Turbo Expo: Power for Land, Sea, and Air, Vol. Volume 1: Aircraft Engine; Ceramics; Coal, Biomass and Alternative Fuels; Controls, Diagnostics and Instrumentation; Education; Electric Power; Awards and Honors, 2009. https://doi.org/10.1115/GT2009-59692, URL https://doi.org/10.1115/GT2009-59692.